ORIGINAL ARTICLE

Effects of Membrane Electrode Assembly Fabrication and Operation Parameters on the Performance of Anion Exchange Membrane Ammonia Electrolyzers

Seokjin Hong[1] · Minwoo Shin[1] · Gyeong Ho Han[1] · Soo Young Kim[2] · Sang Hyun Ahn[1]

Abstract

Compared with conventional oxygen evolution reaction (OER)-paired electrolysis for hydrogen production, ammonia oxidation reaction (AOR)-paired alkaline electrolysis offers enhanced energy efficiency and reduced costs. AOR-paired electrolysis offers a lower theoretical voltage (0.06 V) compared to the OER (1.23 V), enhancing thermodynamic favorability owing to its lower theoretical voltage requirements but faces stability and performance challenges. However, membrane electrode assembly (MEA) fabrication and operational parameter optimization research related to catalyst material development for AOR-paired systems is lacking. In this study, the cell assembly factors, including gasket thickness, compression forces, thermal conditions, and membrane selection, are analyzed, and the electrolyte concentration and electrochemical operating range are optimized for enhanced AOR-paired alkaline electrolysis performance. The optimal gasket thickness and assembly pressure improve the electrical conductivity and reduce the contact resistance. Higher-temperature operation and appropriate anion-exchange membrane screening enhance the ionic conductivity and reaction kinetics. The optimized KOH/NH_4OH electrolyte concentration minimizes catalyst poisoning while maintaining high catalytic activity. Strategic potential window optimization mitigates irreversible surface poisoning while enabling catalyst recovery. Pulsed current protocols eliminate the reverse current phenomenon and electrode degradation by using cyclic voltammetry methods. These integrated optimization strategies enhance the current density performance, demonstrating the viability of AOR-paired electrolysis for practical hydrogen production applications.

Keywords Anion exchange membrane ammonia electrolyzer · Membrane electrode assembly · Poisoning · Surface recovery

Introduction

The rapid increase in energy demand driven by continuous economic growth and population expansion, coupled with the depletion of fossil fuel resources and severe environmental challenges, such as climate change, has highlighted the urgent need to develop and utilize eco-friendly and sustainable energy sources [1]. Renewable energy sources such as solar [2], wind [3], and hydropower [4] have gained significant attention as clean alternatives to fossil fuels. However, they face inherent limitations in providing a stable energy supply owing to their intermittent nature, which depends on the weather conditions and geographical concentration [5]. The development of efficient energy storage and conversion technologies has become essential to overcome the variability of renewable energy and to ensure energy security.

Hydrogen, with its high gravimetric energy density (33.3 kWh kg^{-1} for compressed hydrogen and 8.5 MJ kg^{-1} for liquid hydrogen), has emerged as a clean energy carrier and storage medium that is expected to play a pivotal role in realizing a carbon-neutral society [6]. Hydrogen combustion produces only water without emitting greenhouse gases

✉ Soo Young Kim
sooyoungkim@korea.ac.kr

✉ Sang Hyun Ahn
shahn@cau.ac.kr

1 Department of Chemical Engineering, Chung-Ang University, Seoul 06974, Republic of Korea

2 Department of Materials Science and Engineering, Korea University, Seoul 02841, Republic of Korea

or air pollutants, making it an environmentally friendly alternative to conventional fossil-fuel-based power generation systems when utilized in high-efficiency energy conversion systems such as fuel cells [7]. In particular, hydrogen has a significantly higher energy content in terms of both lower and higher heating values compared to conventional fuels, establishing its recognition as an efficient energy storage medium [8]. In contrast, hydrogen does not exist independently in nature and must be produced through extraction processes from hydrogen-containing compounds such as hydrocarbons or water [9]. Steam methane reforming, currently the most widely used commercial hydrogen production technology, demonstrates high efficiency and economic viability but poses environmental sustainability issues owing to the substantial CO_2 emissions that occur during the production process [10]. Although fuel cell technology has already reached the commercialization stage, large-scale commercial expansion remains limited owing to the lack of hydrogen infrastructure and production cost concerns [11]. Therefore, achieving sustainable hydrogen production technologies without carbon emissions during the production process is urgently required to establish a truly clean hydrogen economy [12].

Among the various hydrogen production technologies, water electrolysis has gained attention as an ideal power-to-gas technology that can store excess electricity generated from renewable energy sources in the form of chemical energy, representing a completely carbon-free, clean hydrogen production technology [13]. Water electrolysis technologies are classified as alkaline water electrolyzer, proton exchange membrane water electrolyzer, and anion exchange membrane water electrolyzer (AEMWE) based on the electrolyte type and operating conditions [14]. Among these, AEMWE has emerged as a next-generation electrolysis technology owing to its advantages of enabling the use of non-noble metal catalysts in alkaline operating environments and significantly reducing the complexity of balance-of-plant systems [15].

Water electrolysis involves the hydrogen evolution reaction (HER) at the cathode and the oxygen evolution reaction (OER) at the anode. The OER requires a substantial overpotential because of its four-electron transfer process and complex reaction mechanism, making it the primary factor that reduces the energy efficiency of the overall system [16]. Recently, research has been actively conducted to replace the anodic OER, which requires a high potential, with more favorable oxidation reactions to reduce the energy required for hydrogen production substantially [17]. In this context, hydrogen production coupled with the ammonia oxidation reaction (AOR) has gained significant attention [18]. Ammonia demonstrates advantageous characteristics as an effective hydrogen carrier because of relatively mild liquefaction

conditions and its requirement of approximately 8 bar of pressure at ambient temperature. This compound exhibits a volumetric hydrogen storage density of 15.6 MJ L^{-1}, representing an advantage over liquid hydrogen storage systems [19]. The theoretical cell potential required for ammonia electrolysis is 0.06 V, approximately 95% lower than the 1.23 V required for water electrolysis, enabling hydrogen production with a significantly reduced theoretical energy input [19]. Furthermore, the AOR produces nitrogen and water through a six-electron transfer process without any CO_2 emissions and can be utilized for ammonia removal from wastewater, making it promising as an environmentally friendly separation and purification process [20].

However, the AOR is a complex electrochemical reaction involving six-electron transfer and multistep reaction pathways, requiring a substantial overpotential beyond the theoretical potential in actual experiments. The reaction proceeds through ammonia adsorption ($NH_{3,ads}$) followed by dehydrogenation by hydroxide ions ($NH_{2,ads}$, NH_{ads}) and N-N bond formation ($N_2H_{x, ads}$) to produce nitrogen [21]. During this process, nitrogen intermediates (NHx and NOx) that accumulate on the catalyst surface cause poisoning, significantly reducing the reaction rate and durability [22].

Among monometallic catalysts, platinum (Pt) exhibits the lowest overpotential and the highest nitrogen selectivity, making it more widely studied than rhodium or palladium for AORs [23]. In particular, the Pt{100} facet demonstrates superior NH_2 adsorption capability compared to the Pt{111} and Pt {110} facets, providing advantages in the initial reaction stage and thereby improving the AOR activity and durability [24]. However, when the limited active sites of platinum are poisoned by nitrogen intermediates, rapid activity loss occurs, which presents a major barrier to industrial applications.

Various strategies have been proposed to address this problem: optimization of the adsorption/desorption balance through surface crystal facet control of platinum nanostructures (nanocubes, nanowires, etc.); enhancement of the electronic structure and poisoning resistance through platinum alloying (PtIrCu, Pt-Zn, etc.) [25, 26] and support introduction (NiFe LDH, graphene oxide, etc.) [27, 28]; and surface regeneration by inducing desorption of poisoning intermediates through electrochemical pulse cycling potential control [29]. Recently, scholars have also investigated securing long-term stability using symmetric electrolyzer designs that can alternately perform OER and HER [30].

In contrast, the research to date has primarily focused on catalyst development, with most studies limited to half-cell testing and lacking performance investigation and optimization at the practical electrolyzer cell level [23, 30]. The thermodynamic advantage of AOR-paired electrolysis originates from its theoretical cell potential of 0.06 V, which is

substantially lower than the 1.23 V required for conventional OER-paired water electrolysis. Despite this significant thermodynamic advantage, practical device performance has been limited, with most research efforts concentrating on catalyst development, often limited to half-cell configurations. This performance gap, and the inherent potential of AOR, is demonstrated by comparing the cell voltage required to achieve a practical current density. For instance, Ham et al. optimized OER-paired AEMWE systems require a cell voltage of approximately 1.6 V_{cell} to deliver current densities in the range of 100–150 mA cm^{-2} [31]. In contrast, AOR-paired electrolyzer literature demonstrates that comparable current densities (15–200 mA cm^{-2}) can be attained at significantly lower potentials, such as 0.6–0.8 V_{cell} [23]. Furthermore, a recent full-cell AOR system achieved 200 mA cm^{-2} at a cell voltage of only 0.7 V [32]. This pronounced operational voltage gap—approximately 1.6 V_{cell} for OER versus 0.7 V_{cell} or less for AOR to achieve similar current density benchmarks—highlights a critical need. It highlights that systematic optimization of the AOR electrolyzer system, including the membrane electrode assembly (MEA) fabrication and operational parameters, is essential to harness this significant potential for reducing costs. However, a few papers have reported the system-level optimization. For the practical application of AOR-paired hydrogen production technology, systematic research at the electrolyzer cell level is essential, requiring performance improvement and economic viability through the optimization of key operating variables such as the electrolyte supply method, operating temperature, and pH.

In this study, we systematically examined how four key parameters affect the performance of an anion exchange membrane ammonia electrolyzer (AEMAE). (1) The effects of the membrane electrode assembly fabrication parameters on the cell construction and contact resistance were analyzed [33]. (2) The effects of the operating temperature on the reaction kinetics were evaluated to understand how the thermal conditions accelerate or hinder electrochemical processes [34]. (3) The membrane–electrolyte interactions, including membrane type and electrolyte concentration, were investigated to determine their effects on the ionic conductivity and transport behavior [35]. (4) The current density and cell voltage were assessed to quantify their roles in controlling the reaction rate and determining the overall cell efficiency [35].

Experimental

MEA Configuration

The MEA was prepared by sandwiching an AEM between a Pt/C/CP anode and cathode with an active area of 1 cm^2. The loading mass of Pt/C/CP (CP: carbon paper, EP4019, and Fuel Cell Earth) with a platinum loading of 0.5 mg cm^{-2} (40 wt%) and an exposed area to the electrolyte of 1.0 cm^2 was sealed. Three different AEMs were evaluated in this study, each requiring specific pretreatment protocols. The Sustainion® X37-50 (Dioxide Materials) was pretreated in 1.0 M KOH at 60 °C for 1 h and immersed in 1.0 M KOH for 24 h, resulting in its conversion into the OH$^-$ form. In contrast, the PiperION and FAA-3-pk130 AEMs were pretreated with 1.0 M KOH for 24 h at room temperature. The gasket thickness was 100–300 μm, and the MEA was assembled at a pressure of 50–60 lb • in. The single-cell temperature was changed from 25 to 80 °C, and the flow rate was 5 cm^3 min^{-1}.

Ammonia Electrolysis Cell Test

The cyclic voltammetry (CV) curves for the AOR were optimized in the lower potential range of −0.25 to −0.75 V_{cell} and the upper potential range of 0.5 to 1.0 V_{cell}. Following the CV measurements, the electrode stability was evaluated using chronoamperometry (CA), chronopotentiometry (CP), stepwise potential, and stepwise current. The CA experiment was performed at 0.6 V_{cell} for 300 s, and the CP test was conducted at 10–100 mA cm^{-2}. The stepwise potential was sequentially maintained at 0.8 V_{cell} for 300 s and −0.65 V_{cell} for 5 s. The stepwise current was sequentially maintained at −50 mA cm^{-2} for 300 s and 100 mA cm^{-2} for 300 s. For all temperature-dependent measurements, the single-cell test station was pre-heated to each temperature (25, 40, 60, and 80 °C) using a heating rod and was allowed to thermally stabilize for 20 min to ensure thermal equilibrium was reached prior to the initiation of any electrochemical measurements.

Results and Discussion

Fewer reports have been published on MEA fabrication and device operation parameters than on catalyst materials for AOR-paired hydrogen production. Hydrogen production *via* an AOR-paired electrolysis system is a practical alternative to production using the conventional OER-paired electrolysis system, and systematic optimization of the fabrication method and operating conditions can further enhance the overall system performance, as shown in Fig. 1.
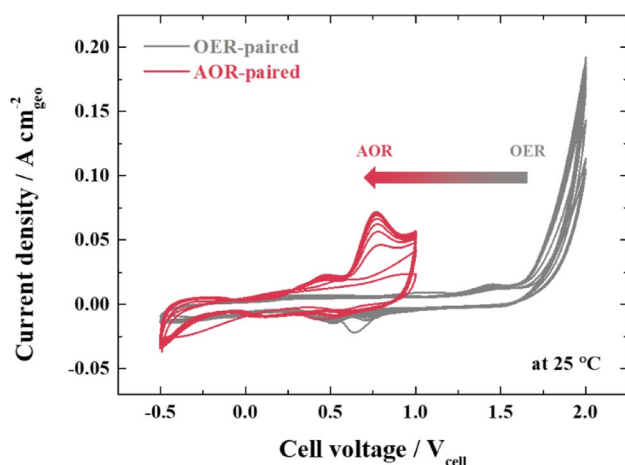
Fig. 1 Comparison of the CV curves with AOR-paired and OER-paired hydrogen production
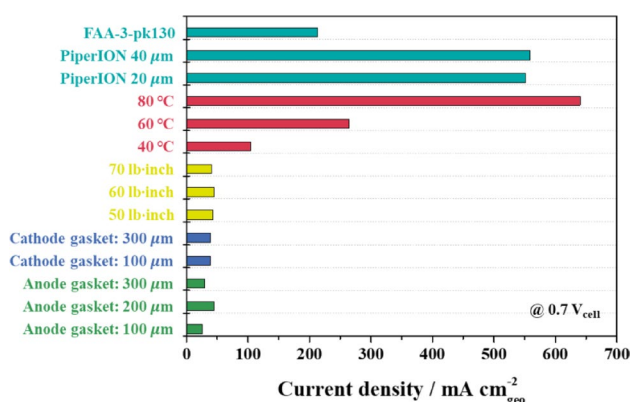
Fig. 2 Current density values at 0.7 V_{cell} during the 20th cycle of CV tests conducted on AEMAE cells from −0.5 to 1.0 V_{cell}. The fabrication protocols and operational parameters are detailed in Table S1

A concise overview of how the electrode fabrication protocol and operational settings govern the hydrogen output in our AEMAE is presented in Fig. 2 and Table S1. Three macroscopic descriptors play dominant roles in the single-cell performance: the apparent charge transfer kinetics, mass-transport characteristics, and ionic conductivity. However, each of these descriptors responds sensitively to the manner in which the catalyst layer is prepared and the selected operating conditions. In particular, the ion conductivity of the membrane varies markedly with the local hydration level and chemical reaction environment formed during operation. As illustrated in Fig. 1; Table S1, appropriate integration of the catalyst-layer architecture, MEA assembly method, and operating parameters led to a roughly 30-fold swing in the current density at 0.7 V_{cell}, from 26 to 761 mA $cm^{−2}$. The specific effects of each variable are discussed in the following Sect. 3.

Optimization of Cell Assembly Parameters of AEMAE

The parameter ranges for this optimization study were based on values from previous AEMWE/AEMAE reports and known material limitations to determine the key parameters affecting performance. The gasket thickness (100–300 μm) and assembly pressure (50–60 lb ● in) ranges were selected based on preliminary screening and conventional MEA fabrication protocols to explore the critical trade-off between contact resistance and mass transport limitations. Similarly, the operating temperature range (25–80 °C) was selected as it represents the conventional operating conditions for AEMWE, balancing kinetic and conductivity gains at high temperatures against the accelerated chemical degradation of AEMs and ionomers often observed above 80–90 °C. The electrolyte concentration ranges (0.5–5.0 M) were selected to cover the typical values reported for AEMWE and AOR, allowing for an investigation of the balance between ionic conductivity and the reported catalyst poisoning at high KOH and ammonia concentrations. While expanding these ranges could potentially identify a different optimum, the selected groups were considered most appropriate for practical, stable AEMAE operation and were sufficient to demonstrate the critical impact of these parameters on performance.

The assembly parameters were systematically evaluated as functions of the gasket thickness, assembly pressure, operating temperature, and membrane type, as shown in Fig. 2. To separate the contribution of the contact resistance between the MEA and bipolar plate, the gasket thickness and assembly compression were optimized. Previous studies of water electrolyzers have shown that excessively thin or thick gaskets lead to increased contact resistance owing to the complex interplay of interfacial and mass transport limitations [36]. When the anode and cathode gasket layers are 100 μm, the cell performance deteriorates; in the case of an ultra-thin gasket, elevated mechanical stress impedes water uptake and release and induces structural damage of the internal components [37]. The electrochemical impedance spectroscopy (EIS) measurements reveal an increase in resistance as the gasket thickness decreases (Figure S1a). Conversely, overly thick gaskets result in diminished internal pressure, which degrades the electrical connectivity between the electrode, catalyst layer, and membrane owing to poor contact resistance [38]. Upon increasing the gasket thickness on both the anode and cathode sides to 300 μm, the AOR activity decreases (Fig. 2), with the EIS results confirming the same trend (Figure S1b). These data indicate that a gasket thickness of 200 μm affords optimal cell performance (Fig. 3a). Additionally, insufficient assembly pressure leads to insufficient contact and elevated resistance, whereas excessive torque promotes mechanical failure

Fig. 3 CV curves of AEMAE cells under varying assembly and operating conditions: (**a**) gasket thickness, (**b**) assembly pressure, (**c**) operating temperature, and (**d**) membrane type
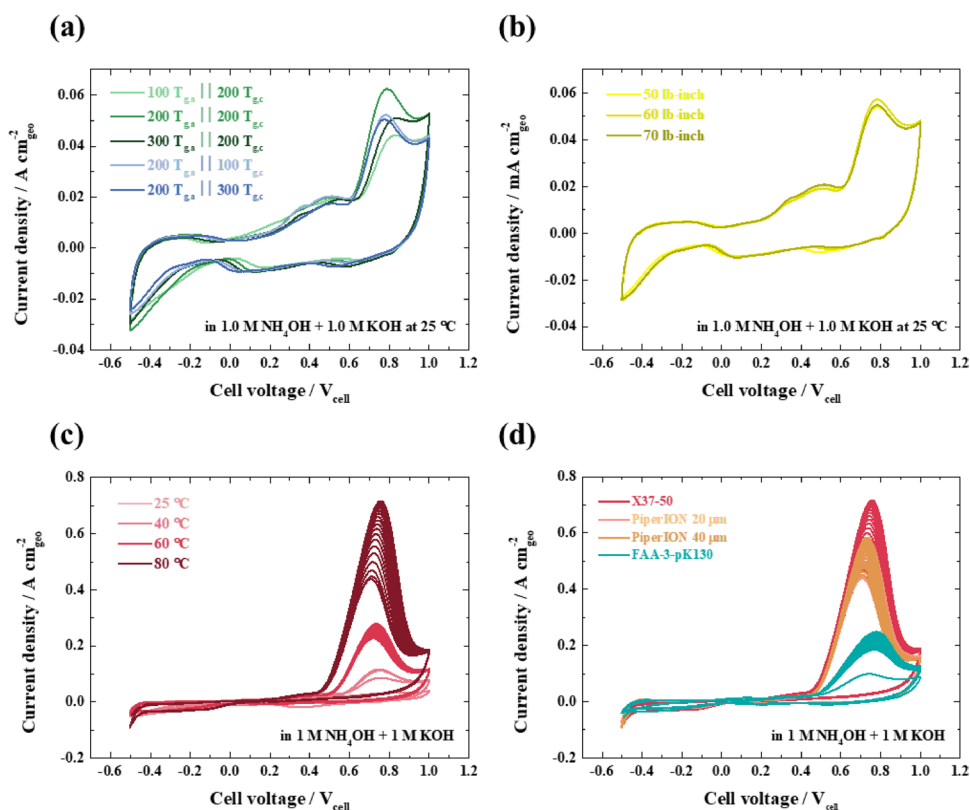
and electrolyte leakage [39]. The highest current density is achieved with an assembly pressure of 60 lb·in, and a similar trend is evident in the EIS results (Figure S2).

This optimization of gasket thickness (200 μm) and assembly pressure (60 lb·in) is critical as it modulates a complex trade-off between ohmic, contact, and mass transport resistances. As supported by studies on AEMWE and PEMWE systems, insufficient compression (e.g., with a 300 μm gasket) maintains the porosity of the catalyst layer but results in poor electrical contact between the gas diffusion layer (GDL), catalyst, and membrane [33, 40]. This leads to high interfacial contact resistance and sub-optimal performance, as confirmed by EIS (Figure S1b). Conversely, excessive compression (e.g., with a 100 μm gasket) minimizes contact resistance but physically collapses the porous structure of the GDL and catalyst layer. This structural deformation severely impedes mass transport, hindering the diffusion of aqueous NH_3 to the active sites (interfacial charge transfer) and the removal of N_2 gas (poisoning by product blockage), thereby increasing the mass transfer resistance. The identified optimum of 200 μm at 60 lb·in represents the point that minimizes the overall impact of these competing resistive losses ohmic resistance, contact resistance, and mass transfer resistance [33]. The current density for the AOR significantly increases with increasing temperature, indicating that the reaction kinetics are rapidly enhanced at elevated temperatures. The highest

current density is observed at 80 °C (Figs. 2 and 3c) [41]. Figure 3c demonstrates that the cycle-to-cycle variation observed at 60 and 80 °C, which is absent at 25 °C, is an intrinsic electrochemical phenomenon and not an effect attributable to the measurement method. This behavior is a known electrochemical activation phase. It is attributed to several competing surface processes whose kinetics—including the primary AOR, $Pt − O/OH_{ads}$ formation, and N − bound poisoning (e.g., N_{ads}) adsorption/desorption—are thermally enhanced at elevated temperatures. These initial sweeps thus represent a conditioning period as the catalyst surface dynamically evolves toward a new, stable cyclic steady state. In contrast, at 25 °C, these same surface rearrangement processes are kinetically hindered, rendering the catalyst surface effectively stable on the timescale of the CV measurement. The significant performance enhancement at elevated temperatures (up to 80 °C, Fig. 3c) is a result of the accelerated kinetics. First, as noted in other AEMWE studies, increasing temperature follows an Arrhenius relationship, accelerating the interfacial charge transfer kinetics of the AOR and HER and thus reducing the activation overpotential [42, 43]. Second, the fundamental ionic conductivity (OH^- mobility) of the AEM (Sustainion® X37-50) and the ionomer within the catalyst layer is enhanced at higher temperatures, reducing the ohmic resistance of the cell [42, 43]. Third, the mass transport of dissolved NH_3 reactant through the electrolyte is improved *via* higher diffusion coefficients.

Notably, this indicates that the desirable AOR pathway and catalyst recovery from poisoning intermediates are accelerated more significantly by temperature than the poisoning pathway, leading to overall improvement in performance across the tested range.

Moreover, the hydroxide ion conductivity varies depending on the type of AEM, with the X37-50 membrane exhibiting the maximum current density for the AOR (Figs. 2 and 3d) [44]. The superior performance of the Sustainion® X37-50 membrane (Fig. 3d) originates from its exceptional ion transport properties. The X37-50 membrane possesses an extremely low area specific resistance of ~ 0.045 $\Omega \bullet$ cm^2 in 1 M KOH and high hydroxide conductivity (80–131 mS cm^{-1}), which minimizes ohmic losses in the cell [45, 46]. The variations in CV peak behavior among the three AEMs arise from their distinct structural characteristics, which influence water management and interfacial kinetics. Both Sustainion® and PiperION are high-conductivity membranes characterized by high water uptake (50–80%), ensuring hydration of the ionomer within the catalyst layer and facilitating efficient OH$^-$ transport to the active sites [45]. The PiperION membrane is based on a functionalized poly(aryl piperidinium) polymer [45]. In contrast, the FAA-3-pk130 membrane is a PEEK/PPO polymer blend, prized for its high dimensional and chemical stability [47, 48]. This rigid structure likely inhibits water management at local mass transport of water and OH$^-$ at the catalyst-ionomer interface. This impedes interfacial charge transfer kinetics and leads to the different CV profile observed. Furthermore, the membranes employ chemically distinct functional groups—poly(aryl piperidinium) in PiperION versus benzyl-ethyl-dimethylammonium in FAA-3-pk130—exhibit different chemical stabilities and create different hydration environments at Pt active sites, explaining the observed electrochemical variation.

Effect of Electrolyte Concentration

The electrochemical performance of the Pt/C/CP catalyst for the AOR was systematically investigated as a function of the KOH and NH$_4$OH concentrations. The CV measurements reveal that the catalytic activity gradually increases with increasing KOH concentration up to 1.0 M, beyond which a declining trend in performance is observed (Fig. 4a). The results of the CA experiments conducted at 0.6 V$_{cell}$ demonstrate that the poisoning effects diminish and electrode stability improves with increasing KOH concentration up to 1.0 M, whereas concentrations exceeding 1.0 M result in accelerated activity degradation due to poisoning (Fig. 4b). The results of the CP test at an applied current of 50 mA cm^{-2} exhibit a potential jump to the OER at ~1200 s, with optimal long-term stability at a KOH concentration of 1.0 M (Fig. 4c). The observation of more rapid potential jumps at KOH concentrations above 1.0 M suggests that elevated hydroxide ion concentrations contribute to catalyst surface poisoning by enhancing OH adsorption.

Fig. 4 Influence of anolyte KOH concentration on AEMAE cell performance: (**a**) CV results for Pt/C/CP, (**b**) results of CA test for 600 s, (**c**) results of CP test for 1500 s, and (**d**) Nyquist plot at 0.6 V$_{cell}$
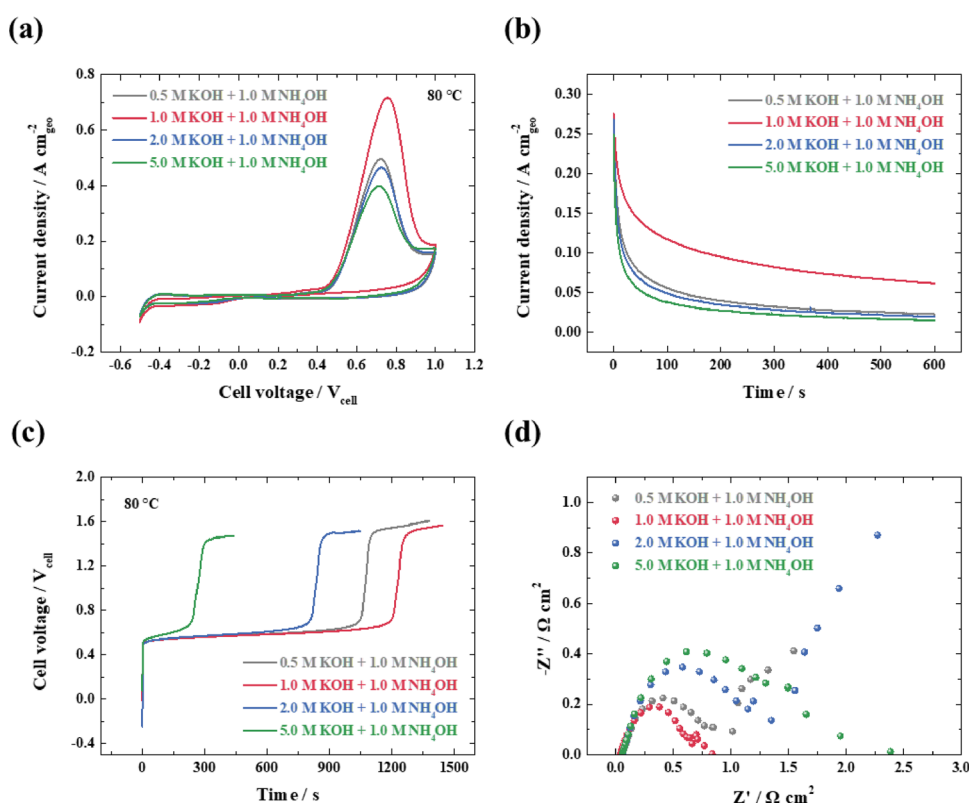
The EIS measurements at 0.6 V_{cell} confirm that the lowest charge-transfer resistance occurs at a KOH concentration of 1.0 M.

Subsequently, the influence of the NH_4OH concentration on the AEMAE performance was evaluated while maintaining a fixed KOH concentration of 1.0 M. An optimal KOH concentration of 1.0 M reflects a fundamental trade-off at the catalyst-electrolyte interface. The AOR relies on both adsorbed NH_3 and OH^- ions for its multi-step mechanism. At low KOH concentration (< 1.0 M), the reaction is predominantly limited by the availability of OH^- ions, reflected in increased charge transfer resistance (Fig. 4d). Conversely, at high KOH concentration (> 1.0 M), the Pt catalyst surface becomes saturated with competitively adsorbed hydroxide ions OH_{ads}. These non-reactive species block the active sites required for the initial adsorption of NH_3, effectively poisoning the catalyst *via* site-blocking and inhibiting the overall AOR rate, leading to the observed performance decline (Fig. 4a–c).

The CV analysis results indicate that NH_4OH concentrations of up to 1.0 M result in enhanced catalytic activity, followed by performance degradation at higher concentrations (Fig. 5a). The results of the CA tests at 0.6 V_{RHE} similarly demonstrate minimized poisoning effects and improved stability with increasing NH_4OH concentration up to 1.0 M, whereas concentrations above this threshold lead to accelerated poisoning-induced activity loss (Fig. 5b). The CP measurements at an applied current density of 50 mA cm^{-2}

reveal potential jumps in the OER at ~1200 s, with comparable long-term stability observed at NH_4OH concentrations of both 1.0 M and 2.0 M (Fig. 5c). Figure 5c highlights an important distinction between kinetic and mass-transport limitations. The optimized condition of 1.0 M NH_4OH is based on potentiostatic (CV, CA) and EIS data in Figs. 5a–d, which are most sensitive to interfacial kinetics. These results demonstrate that 1.0 M provides the lowest charge-transfer resistance (Fig. 5d) and highest kinetic stability against poisoning (Fig. 5b) at a fixed potential. However, the CP test in Fig. 5c is galvanostatic, maintaining a fixed current of 50 mA cm^{-2} and thus introducing reactant mass transport as a joint limitation. The comparable long-term stability of the 2.0 M NH_4OH, which appears to contradict the kinetic data, reflects a competitive adsorption trade-off between NH_3 supply and N_{ads} accumulation. The 2.0 M NH_4OH maintains sufficient ammonia availability to suppress OH^- adsorption, enabling the 50 mA cm^{-2} current density. The 1.0 M NH_4OH, while kinetically superior, becomes mass-transport limited at this high NH_4OH concentration, allowing OH^- to preferentially occupy active sites. Thus, the two anolyte conditions transition to OER *via* different mechanisms: the 1.0 M becomes mass-transport limited (triggering OH^- adsorption at ~1200 s), while the 2.0 M is limited by its higher intrinsic kinetic poisoning rate (~1400 s). The sharp potential jump at 5.0 M NH_4OH confirms that excessive concentrations accelerate N_{ads} poisoning. Therefore, 1.0 M NH_4OH remains the energy-efficient optimum, as it

Fig. 5 Influence of anolyte NH_4OH concentration on AEMAE cell performance: (**a**) CV results for Pt/C/CP, (**b**) results of CA test for 600 s, (**c**) results of CP test for 1500 s, and (**d**) Nyquist plot at 0.6 V_{cell}
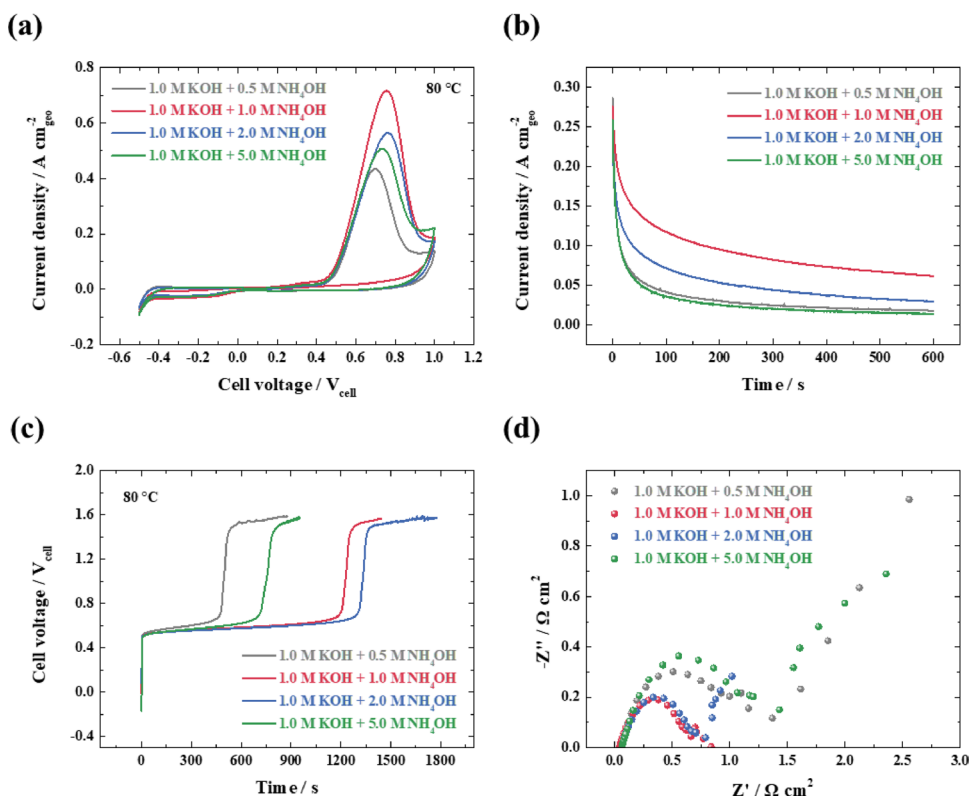
operates at significantly lower cell voltage throughout its lifetime, minimizing electrical energy consumption despite earlier mass-transport limitation. The EIS analysis results at 0.6 V_{cell} confirm the minimal charge transfer resistance at an NH$_4$OH concentration of 1.0 M (Fig. 5d). The 1.0 M NH$_4$OH concentration represents a balance between reactant supply and surface poisoning. At this concentration, higher NH$_4$OH levels accelerate the mass transport rate of NH$_3$ to the catalyst (improving charge transfer kinetics), yet simultaneously promote the formation of nitrogen-containing intermediates NH$_{x, ads}$ and N$_{ads}$. As these intermediates represent the primary poisoning species for Pt-based AOR, their rapid accumulation at concentrations above 1.0 M, blocking active sites and causing the rapid activity loss seen in the CA tests (Fig. 5b). The 1.0 M concentration thus represents the optimal balance, maximizing reactant availability while minimizing irreversible N$_{ads}$ poisoning, as confirmed by the minimal charge transfer resistance in the EIS data (Fig. 5d).

Influence of Electrochemical Electrolyzer Operating Conditions

To establish the optimal electrochemical operating conditions for the AEMAE, systematic investigations were conducted by varying the upper and lower potential limits in the CV experiments (Fig. 6). Previous studies have demonstrated that the reduction current peaks observed in the low-potential region (≤ -0.25 V_{SHE}) correspond to N$_{ads}$ species on the platinum surface, which exhibit irreversible behavior once formed [49]. Although oxide species (OH$_{ads}$/Pt-oxide) represent nontoxic intermediates that can
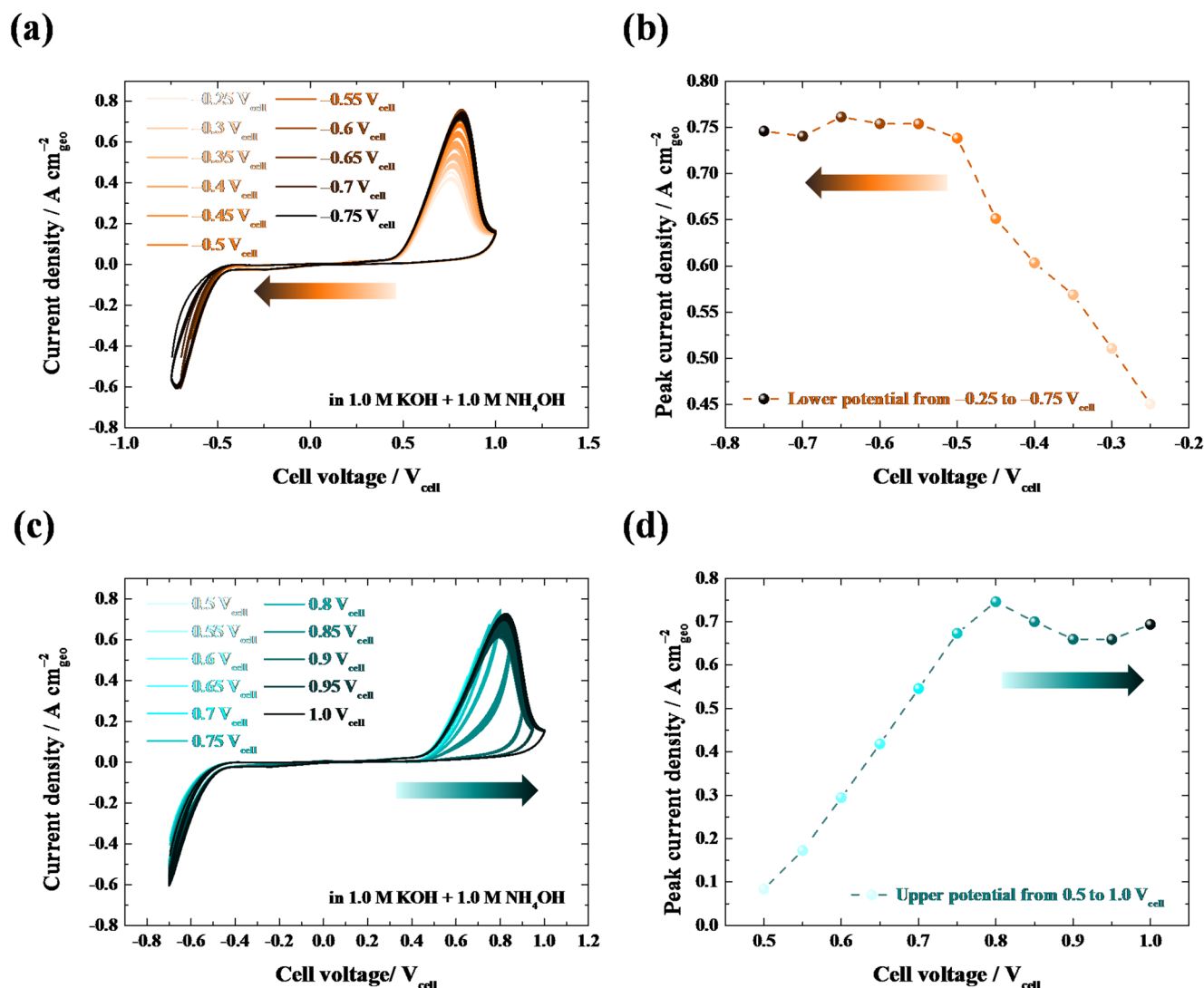
Fig. 6 Comparison of the lower and upper potential limits of the CV curves in 1.0 M NH$_4$OH+1.0 M KOH. (**a**) CV curves of lower potential change from -0.05 to -0.75 V_{cell}, and (**b**) peak current density corresponding to lower potential change of (a). (**c**) CV curves of lower potential change from 0.5 to 1.0 V_{cell}, and (**d**) peak current density corresponding to lower potential change of (c)

be reversibly reduced and recovered, irreversible poisoning by N_{ads} cannot be eliminated merely through potential window modifications. The electrochemical results presented in Fig. 6a and b reveal that shifting the lower potential toward a more negative potential gradually enhances the catalyst surface recovery, resulting in increased current densities of ammonia oxidation. However, operation beyond -0.75 V_{cell} in the negative potential region results in diminished AOR performance, indicating an optimal lower potential threshold. The influence of the upper potential variations on N_2 formation was systematically examined to elucidate the effects of gradual platinum surface oxidation and reduction processes [36]. Below 0.65 V_{cell}, the forward and reverse scans demonstrate complete overlap without detectable hysteresis, signifying reversible N_2 generation in the absence of platinum oxide formation (Fig. 6c and d). Conversely, at potentials exceeding 0.75 V_{cell}, substantial variation between the forward and backward scan profiles becomes apparent, which is attributed to the formation of platinum oxides that impede the active sites responsible for ammonia adsorption and subsequent dehydrogenation to N_2 [50]. The maximum AOR current density is achieved at an upper potential of 0.8 V_{cell}, whereas potentials above 0.85 V_{cell} result in almost complete inhibition of N_2 generation due to extensive platinum oxide layer formation. Consequently, a lower potential of -0.75 V_{cell} and an upper potential of 0.8 V_{cell} can be identified as the optimal electrochemical operating conditions, representing the optimal potential window for sustained ammonia electrooxidation performance.

Optimization of Pulsed Current Operation for Sustainable Hydrogen Production

Through optimization of the upper and lower potentials, the optimal voltage conditions were determined for hydrogen production *via* the AOR and catalyst recovery from surface poisoning. For sustained hydrogen production, the results of a pulsed current test were compared with those obtained using the on-off cycling protocol (Fig. 7). To determine the optimal operating parameters, CP measurements were conducted over a temperature range of 25–80 °C under an applied current density of 0.05 A cm^{-2}. Below 60 °C a potential jump toward the OER is observed within 100 s, whereas at 80 °C a stable AOR is maintained for 1300 s (Fig. 7a). Based on the stepwise current density test results, we identified 80 °C at 50 mA cm^{-2} as optimal. To achieve continuous hydrogen production, experiments were designed to alternate between the AOR and catalyst surface recovery (Fig. 7c). Previous durability tests employed on/off protocols and demonstrated stable performance without potential jumps [51]. As shown in Fig. 7c 0.05 A cm^{-2} was applied for 300 s in the upper current regime, followed by a shutdown

period of either 5–300 s. Under the 5 s-off shutdown condition, a potential jump occurs at the sixth cycle (1400 s), and the 60 s-off shutdown condition yields a similar behavior at the fifth cycle (1800 s). Both shutdown protocols result in gradual potential increases during consecutive upper-current intervals. Notably, a reverse current phenomenon emerges during the shutdown period. This reverse-current phenomenon results from galvanic cell formation, which maintains potential differences even after power termination [52]. Such current switching induces cathode oxidation in a reductive environment and anode reduction in an oxidative state, causing electrode degradation. Consequently, pulsed-current protocols were applied to ensure stable system operation for sustained hydrogen production (Fig. 7c). The methodology alternated between the upper current (0.05 A cm^{-2}, 300 s) and lower current (-0.05 A cm^{-2}, 5 s), demonstrating stable cycling reproducibility without a potential rise over 3600 s.

Conclusions

Systematic optimization of the MEA fabrication and operating parameters in an AOR-paired alkaline electrolyzer significantly improves the hydrogen production performance. This study was structured as a parameter-by-parameter investigation to first establish an operational baseline. By tailoring the physical assembly, an optimal 200 μm gasket and 60 lb·in pressure were found to balance the trade-off between ohmic, contact, and mass transport resistances. Concurrently, enhancing the kinetics and ionic conductivity (80 °C, X37-50 AEM) and tailoring the electrolyte (1.0 M KOH/1.0 M NH$_4$OH) to minimize catalyst poisoning while maximizing reactant availability were critical. The integration of these individually optimized parameters yielded a 30-fold enhancement in current density at 0.7 V_{cell}, from 26 to 761 mA cm^{-2}. This substantial improvement demonstrates the potent combined effect of these factors. Furthermore, electrochemical protocols were established wherein an optimal potential window (-0.75 to 0.80 V_{cell}) suppresses irreversible N_{ads} poisoning while enabling reversible platinum oxide recovery, and implementing a pulsed current protocol (0.05 A cm^{-2} for 300 s and -0.05 A cm^{-2} for 5 s) results in steady ammonia oxidation without a potential jump for more than 3600 s. These integrated improvements provide a foundation for subsequent studies to quantify the specific interactive effects between these variables. This demonstrates a compelling, energy-efficient alternative to traditional OER-paired electrolysis for sustainable hydrogen production.
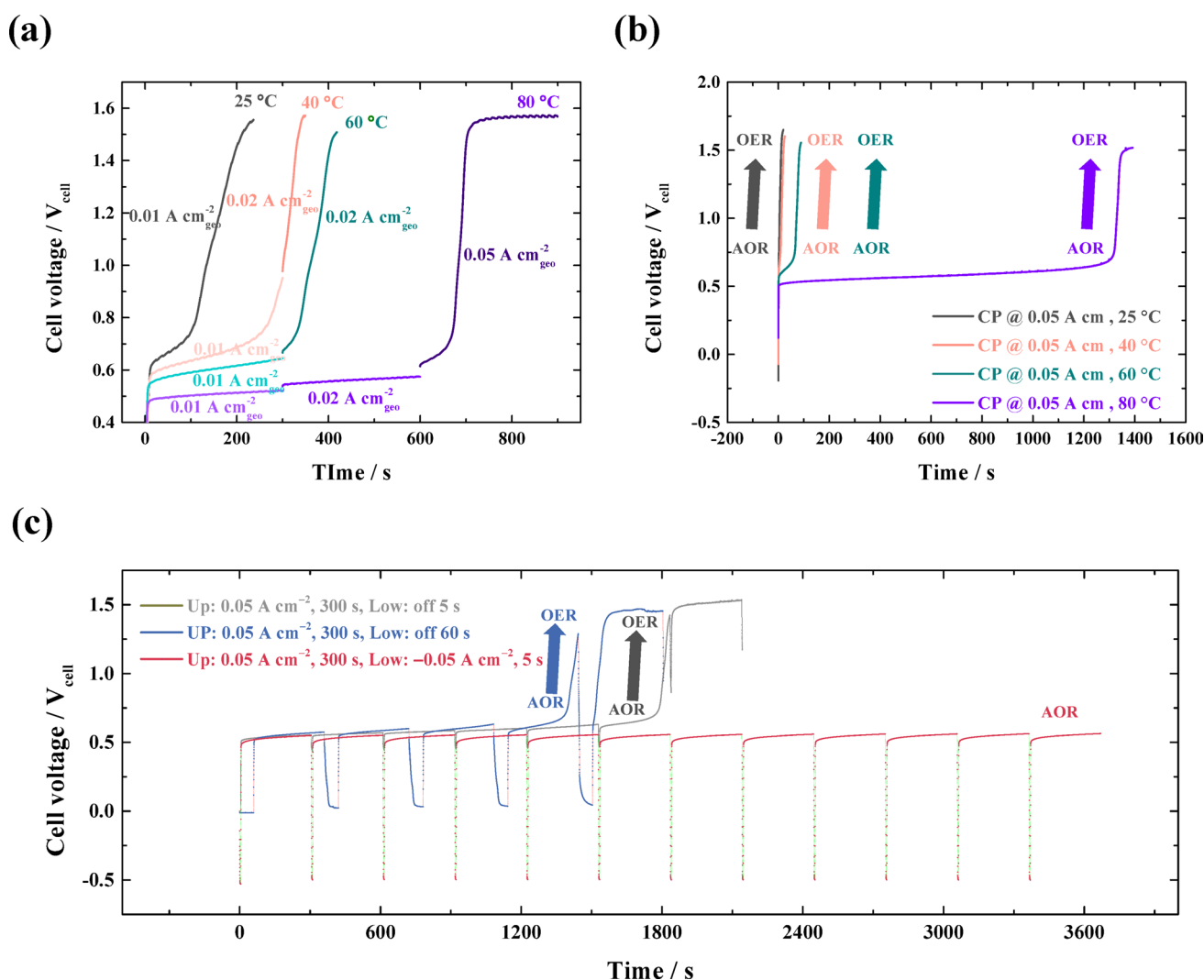
Fig. 7 Results of (**a**) stepwise CA test from 10 to 50 mA cm^{-2} for 300 s, (**b**) CA test at 0.05 A cm^{-2}, and (**c**) pulsed stability test of on-off step and pulsed current step

Declarations

Conflict of interest The authors declare that they have no competing financial or personal relationships that may have influenced the work reported in this paper.

References

1. C.C. Elam, C.E.G. Padró, G. Sandrock, A. Luzzi, P. Lindblad, E.F. Hagen, Int. J. Hydrog Energy. **28**, 601 (2003)
2. C. Rae, F. Bradley, Renew. Sustain. Energy Rev. **16**, 6497 (2012)
3. E. Kabir, P. Kumar, S. Kumar, A.A. Adelodun, K.-H. Kim, Renew. Sustain. Energy Rev. **82**, 894 (2018)
4. M. Götz, J. Lefebvre, F. Mörs, A.M. McDaniel Koch, F. Graf, S. Bajohr, R. Reimert, T. Kolb, Renew. Energy **85**, 1371 (2016)
5. N.A.S. Amin, T.C. Yaw, Int. J. Hydrogen Energy **32**, 1789 (2007)
6. P.P. Edwards, V.L. Kuznetsov, W.I.F. David, Philos. Trans. A Math. Phys. Eng. Sci. **365**, 1043 (2007)
7. M.K. Singla, P. Nijhawan, A.S. Oberoi, Environ. Sci. Pollut. Res. Int. **28**, 19536 (2021)
8. J. Bai, D. Liu, J. Yang, Y. Chen, ChemSusChem. **12**, 2117 (2019)
9. M. Ball, M. Wietschel, Int. J. Hydrogen Energy **34**, 615 (2009)
10. C.C. Chu, M.D. Suhainin, D.N.H.A.P.H.O. Ali, J.Y. Lim, P.S. Swee, J.Y. Raymundo, R.X.H. Tan, M.K. Yap, H.F. Khoo, H. Suhaimi, P.E. Abas, Hydrogen. **6**, 23 (2025)
11. J. Garche, L. Jürissen, Electrochem. Soc. Interface **24**, 39 (2015)
12. K. Dillman, J. Heinonen, Climate. **11**, 25 (2023)

13. A.J. Shih, M.C.O. Monteiro, F. Dattila, D. Pavesi, M. Philips, A.H.M. da Silva, R.E. Vos, K. Ojha, S. Park, O. van der Heijden, G. Marcandalli, A. Goyal, M. Villalba, X. Chen, G.T.K.K. Gunasooriya, I. McCrum, R. Mom, N. López, M.T.M. Koper, Nat. Rev. Methods Primers **2**, 84 (2022)

14. T. Lim, S.-K. Kim, Chem. Eng. J. **433**, 133681 (2022)

15. S. Shaik, J. Kundu, Y. Yuan, W. Chung, D. Han, U. Lee, H. Huang, S.-I. Choi, Adv. Energy Mater. **14**, 2401956 (2024)

16. X. Li, X. Hao, A. Abudula, G. Guan, J. Mater. Chem. A **4**, 11973 (2016)

17. L. Du, Y. Sun, B. You, Energy. **1**, 100004 (2021)

18. F. Vitse, M. Cooper, G.G. Botte, J. Power Sources **142**, 18 (2005)

19. Y. Yang, J. Kim, H. Jo, A. Seong, M. Lee, H.-K. Min, M.-g Seo, Y. Choi, G. Kim, J. Mater. Chem. A **9**, 11571 (2021)

20. J. Shu, R. Liu, Z. Liu, J. Qiu, H. Chen, C. Tao, Environ. Technol. **38**, 370 (2017)

21. J.H. Jang, S.Y. Park, D.H. Youn, Y.J. Jang, Catalysts. **13**, 803 (2023)

22. X. Xi, Y. Fan, K. Zhang, Y. Liu, F. Nie, H. Guan, J. Wu, Chem. Eng. J. **435**, 134818 (2022)

23. H. Kim, S. Hong, H. Kim, Y. Jun, S.Y. Kim, S.H. Ahn, Appl. Mater. Today **29**, 101640 (2022)

24. S.W. Wallace, I.T. McCrum, M.J. Janik, Catal. Today **371**, 50 (2021)

25. X. Lin, X. Zhang, Z. Wang, X. Zhu, J. Zhu, P. Chen, T. Lyu, C. Li, Z.Q. Tian, P.K. Shen, J. Colloid Interface Sci. **601**, 1 (2021)

26. M.A. Matin, S. Kim, Y. Kim, C. Han, S. Byun, H.C. Kim, J. Power Sources **591**, 233885 (2024)

27. J. Lee, S.A. Lee, J. Kim, T.H. Lee, W.S. Cheon, S. Choi, S.H. Park, H.W. Jang, Appl. Catal. B **371**, 125251 (2025)

28. S.S.P.R. Rahardjo, Y.-J. Shih, Chem. Eng. J. **473**, 145396 (2023)

29. N.M. Adli, H. Zhang, S. Mukherjee, G. Wu, J. Electrochem. Soc. **165**, J3130 (2018)

30. H. Ju, D. Yoon, S. Bong, J. Lee, Curr. Opin. Electrochem. **49**, 101609 (2025)

31. H. Ham, S. Hong, S. Kang, K. Cho, J. Lee, Acs Energy Lett. **6**, 364 (2021)

32. O. Gecgel, C.E. Alvarez-Pugliese, J. Solis, G.G. Botte, Int. J. Hydrogen Energy **141**, 1349 (2025)

33. A. Lim, H. Kim, D. Henkensmeier, S.J. Yoo, J.Y. Kim, S.Y. Lee, Y.-E. Sung, J.H. Jang, H.S. Park, J. Ind. Eng. Chem. **76**, 410 (2019)

34. S. Xing, C. Zhao, W. Liu, J. Zou, M. Chen, H. Wang, Appl. Energy **303**, 117632 (2021)

35. Z. Liang, L. Song, Z. Ma, Y. Zhang, R.R. Adzic, J.X. Wang, ECS Trans. **85**, 161 (2018)

36. Z.-F. Li, Y. Wang, G.G. Botte, Electrochim. Acta **228**, 351 (2017)

37. S. Siracusano, A. Di Blasi, V. Baglio, G. Brunaccini, N. Briguglio, A. Stassi, R. Ornelas, E. Trifoni, V. Antonucci, A.S. Aricò, Int. J. Hydrogen Energy **36**, 3333 (2011)

38. S. Shin, S. Park, Y.R. Lee, Y. Shin, D.M. Yu, S.J. Yoon, H.Y. Jeong, T.-H. Kim, H. Han, Y.-E. Sung, S. Kim, J. Am. Ceram. Soc., **108**, e20648 (2025)

39. Q. Xu, S.Z. Oener, G. Lindquist, H. Jiang, C. Li, S.W. Boettcher, ACS Energy Lett. **6**, 305 (2021)

40. M.R. Parimuha, J.L. Young, J.K. Lee, A. Yilmaz, S. Diaz-Abad, R. Gawas, T. Schuler, S.K. Babu, G. Bender, Int. J. Hydrogen Energy **114**, 486 (2025)

41. H.S. Pillai, Y. Li, S.-H. Wang, N. Omidvar, Q. Mu, L.E.K. Achenie, F. Abild-Pedersen, J. Yang, G. Wu, Nat. Commun. **14**, 792 (2023)

42. G. Lee, S.E. Jun, J. Lim, J. Kim, H. Lee, W.S. Cheon, G.W. Ryoo, B.-G. Cho, S. Lee, M.S. Kwon, I.-H. Park, H.W. Jang, S.H. Park, K.C. Kwon, Adv. Sci. **12**, 2414622 (2025)

43. S. Hong, H. Kim, G.H. Han, J. Yoo, S.-K. Kim, J.H. Jang, S.H. Ahn, Chem. Eng. J. **500**, 15 (2024)

44. Y. Li, H.S. Pillai, T. Wang, S. Hwang, Y. Zhao, Z. Qiao, Q. Mu, S. Karakalos, M. Chen, J. Yang, D. Su, H. Xin, Y. Yan, G. Wu, Energy Environ. Sci. **14**, 1449 (2021)

45. S. Garg, C.A.G. Rodriguez, T.E. Rufford, J.R. Varcoe, B. Seger, Energy Environ. Sci. **15**, 4440 (2022)

46. F.-F. Su, H.-H. Yu, H. Yang, Membranes. **14**, 246 (2024)

47. A. Giovanelli, A. Pozio, A. Pucci, M. Geppi, F. Martini, Polymer. **311**, 127536 (2024)

48. H. Khalid, M. Najibah, H.S. Park, C. Bae, D. Henkensmeier, Membranes **12**, 989 (2022)

49. Y. CaoYu, Y. Guo, Z. Hu, F. Gui, Y. Lei, J. Ni, C. Zhang, Q. Xiao, Energy Fuels **38**, 14645 (2024)

50. S.I. Venturini, D.R.M. Martins, de Godoi, J. Perez, ACS Catal. **13**, 10835 (2023)

51. D. Yoon, S. Chung, M. Choi, E. Yang, J. Lee, J. Energy Chem. **93**, 352 (2024)

52. Y. Kim, S.-M. Jung, K.-S. Kim, H.-Y. Kim, J. Kwon, J. Lee, H.-S. Cho, Y.-T. Kim, JACS Au. **2**, 2491 (2022)